System Equivalent Flux Density of LWA1 Beams

v1: July 28, 2014

Frank Schinzel (UNM), Emil Polisensky (NRL)

1 Introduction

This document is a summary of recent work to determine the system equivalent flux densities (SEFD) of the beam-formed aperture array LWA1. The various aspects of the SEFD of LWA1 were presented in Ellingson et al. (2013) based on a limited number of measurements and were discussed in more general terms for LWA-type aperture arrays in Ellingson (2011). Here, the analysis of the station beam SEFD is expanded based on over 400 beam hours of drift scan observations of Cygnus A, Cassiopeia A, Taurus A, and Virgo A. The observations were carried out between August 4th and November 12th 2013 using LWA1 custom beam-formed DRX data as well as regular full-polarization beam-formed data. The custom beam-formed observing mode enables simultaneous observation with the LWA1 beam-formed array and that of a single dipole allowing correlation with outrigger #4 (stand 258) forming an East-West baseline of 340 m. Observations in this mode allow the determination of beam-formed SEFDs along with that of a single E-W baseline in order to estimate the contribution of added sky noise and large scale diffuse emission in beam-formed observations. The observations were carried out with the split bandwidth filter attenuating emission below 30 MHz and with two 19.6 MHz tunings with the center frequencies set to 42.0 and 74.0 MHz.

The custom beam-formed data contains the dipole data in one of the polarizations and beam-formed data in the other polarization of the data output. After recording the data are correlated using the software correlator implemented in the LWA software library (LSL) which calculates the correlation and autocorrelation products of the 2-element interferometer between beam and dipole assuming a phase center at zenith. In order to correct the correlated visibilities for the position of the target object (fringe stopping), the visibilities are shifted accordingly. Resulting visibilities of the correlation, as well as the autocorrelation product of the beam, are used for further analysis. Figure 1 shows an example waterfall plot of the real part of the visibilities for one frequency tuning of Cygnus A before and after the phase correction was applied. A second correction that is applied is related

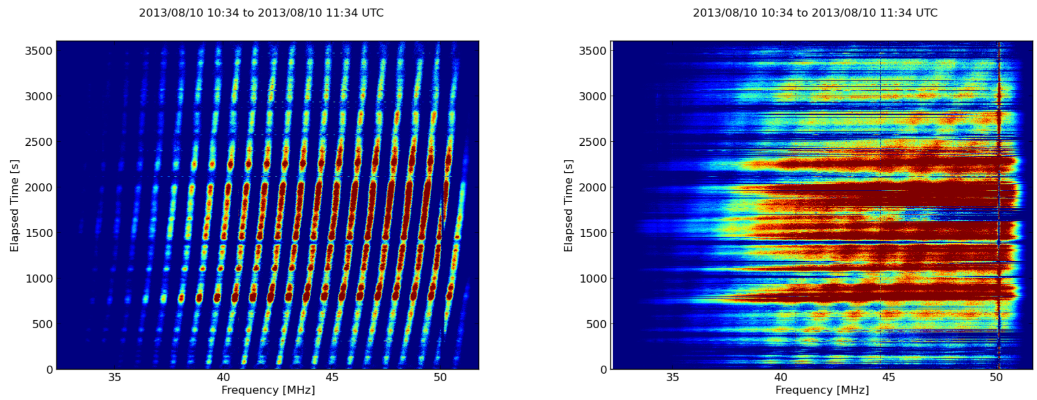

Figure 1: *Left:* Waterfall plot of the real-part of the visibilities of a XX polarization observation of Cygnus A with the two-element interferometer beam-outrigger at 30 degrees elevation. *Right:* Waterfall plot of the same dataset after fringe stopping was applied to the visibilities.

to the wide bandwidth. Delays are calculated for the center frequency only which introduces a constant phase slope in the calculated solution. This phase slope is determined and removed as well.

The raw time-series full polarization beam-formed data is converted to a spectrometer file using scripts from the LSL Commissioning extension. All Stokes parameters (I,Q,U, and V) are calculated, allowing future polarization analysis of this dataset.

In order to extract values from the dataset the phase shifted data was taken and time-series were extracted for select frequencies averaging over 1 MHz of bandwidth around each. For determination of the SEFD on-source and off-source values need to be determined. The off-source value is determined by selecting a time interval of 4 min where the observed power was minimal and calculating its mean value and standard deviation. For determining the on-source value, a 6-th order polynomial is fitted around the time of the transit. The width of the fitting region is varied with the expected frequency dependence of the beam-width. A polynomial fit turned out to produce more reliable fitting results than a Gaussian function. The statistical error of the peak value from the fit is determined by subtracting the fit from the data and calculating the standard deviation for a 4 min period around the peak value of the fit.

2 System Equivalent Flux Density

The SEFD in the direction of Cygnus A, Cassiopeia A, Taurus A, and Virgo A were determined using the setup described in Section 1. The beam was fixed to a position close to transit for each object and the sky was allowed to drift through the beam. Each observation was started 1.5 hours before a given object passed through the center of the beam and ended half an hour after. The respective pointings are listed in Table 1 together with the target source flux densities. The target flux densities were obtained from the interpolated values of the VLSS bright source spectral flux calibrators[1]. For Cassiopeia A three flux density values are listed in Table 1, the one obtained from the VLSS bright source spectral flux calibrators, a predicted value of the observing epoch 2013.86 corrected for a secular decrease of 0.8% year^{-1} (Helmboldt & Kassim 2009), and an observed value obtained through the observed flux density ratio between Cygnus A and Cassiopeia A for which an average flux density ratio (Cyg A/Cas A) of 1.11 was determined. In the following analysis we use the observed flux density values of Cas A.

Table 1: Pointings and target flux densities.

Target	Alt.	Az.	36	42	48	68	74	80
		deg.			MHz/kJy			
Cyg A	80.0	314.9	26.065	24.046	22.235	18.127	17.250	16.479
Cas A (1965.0)	65.0	5.5/354.6	37.265	33.726	30.686	23.984	22.591	21.379
Cas A (2013.86)^p			22.747	20.586	18.731	14.640	13.790	13.221
Cas A (2013.86)^o			23.482	21.663	20.032	16.331	15.540	13.846
Tau A	75.0	219.0	2.629	2.468	2.336	2.025	1.956	1.894
Vir A	65.0	147.1	3.957	3.426	2.895	1.865	1.676	1.519

Notes:
^{p} – predicted
^{o} – observed

The SEFD was then determined using the following equation (Ellingson et al. 2013):

$$SEFD = S\left(\frac{P_1}{P_0} - 1\right)^{-1}, \tag{1}$$

where S is the target flux density, P_1 is the peak power and P_0 is the off-peak power of the drift scan. For the analysis the power was determined averaging a bandwidth of 1 MHz around the following frequencies: 36.0, 42.0, 48.0, 68.0, 74.0, and 80.0 MHz. The peak power, P_1, was determined from a polynomial fit as described in Section 1, the off-peak power, P_0, was determined from the same position in the sky for a 4 min interval about 1.5 hours before the target drifts through the beam. The standard deviation of the data over which the off-peak power was determined was calculated and provides a statistical estimate on the error of the measurement. Systematic errors of the measurement are not accounted for.

Tables 2 and 3 show the respective SEFD values determined with this method for the beam+beam autocorrelation and the beam+outrigger correlation. The resulting values are

[1]http://www.nrl.navy.mil/rsd/vlss/calspec/

plotted in Fig. 2 against frequency for illustrative purposes. The observations of Cygnus A reported here were taken on November 12, 2013. Values reported for Cas A were observed on November 12 and September 26, 2013 providing consistent results. Observations of Tau A and Vir A were taken on September 21 and 26, 2013. Unfortunately, the outrigger-LWA1 baseline showed strong scintillations in the 74 MHz tuning, increasing the statistical error bars. Strong RFI was also present during the transit of the observation in the low frequency tunings. Despite this, consistent values that are comparable to Cygnus A and Cassiopeia A were obtained from these observations. Comparison with the values reported in Ellingson et al. (2013) the here presented values are more consistent and about a factor of 2 smaller than what was previously reported.

From the compilation of these SEFD values the following observations can be made:

- Ionospheric scintillation and RFI can have a significant impact on the obtained SEFD values (see e.g. Cas A outrigger-beam correlations). This effect will be addressed in a future memo on stability of measurements over longer periods of time.

- The SEFD value at 36 MHz is systematically higher than at other frequencies. This is due to the filter roll-off in the ARX split bandwidth mode that attenuates low frequencies and reduces the chance of interference from below 30 MHz.

- Observing different parts of the sky results in different SEFD values for the beam autocorrelation. The SEFD is higher when the Galactic plane is up (Cyg A, Cas A) with values around 11–15 kJy compared to 5–7 kJy when the Galactic plane is down (Vir A, Tau A).

- The SEFD values determined for the beam-outrigger baseline are less dependent on the sky position from which the values were bootstrapped. Overall the SEFD for this baseline is up to a factor of 7 more sensitive than the beam alone (in the case of Vir A).

- From this limited set of observations it seems that SEFD values determined from Cygnus A and Virgo A are the most reliable and show a more or less flat SEFD dependence with frequency between 42 and 74 MHz.

3 Elevation Dependent Gain

In this section the elevation dependence of the measured power of a bright calibrator source is evaluated. For this a range of drift scan observations of Cygnus A, Cassiopeia A, Taurus A, and Virgo A were conducted sampling all observerable elevations in 5° steps. Most observations were performed for Cygnus A and Cassiopeia A which at the time of the observations were observable at night time. Considerably less observations were performed for Taurus A and Virgo A which were observed during daytime with a less smooth ionosphere which mainly impacted longer baselines. Observations were performed in regular

Table 2: SEFDs derived from the beam autocorrelation. Errors are statistical only.

Target	Pol.	36	42	48	68	74	80
		MHz/kJy					
Cyg A	XX	13.9±1.2	10.86±0.55	10.78±0.41	9.88±0.27	10.21±0.23	10.59±0.19
Cyg A	YY	13.7±1.2	10.75±0.58	10.67±0.47	10.33±0.27	10.89±0.24	11.33±0.20
Cas A[1]	XX	16.94±0.79	15.00±0.47	13.45±0.26	10.79±0.19	11.33±0.18	12.21±0.18
Cas A[1]	YY	16.32±0.74	14.50±0.44	12.95±0.26	8.50±0.15	8.58±0.13	8.82±0.14
Cas A[2]	XX	16.3±1.3	14.45±0.72	14.54±0.49	11.98±0.33	12.68±0.35	13.00±0.67
Cas A[2]	YY	14.8±1.1	13.67±0.64	13.90±0.44	9.08±0.25	9.37±0.29	9.52±0.25
Tau A	XX	6.32±0.33	5.05±0.22	5.02±0.17	8.64±0.26	9.22±0.21	10.15±0.24
Tau A	YY	5.93±0.31	4.79±0.20	4.96±0.17	7.77±0.20	8.64±0.22	9.68±0.67
Vir A*	XX	9.36±0.72	7.2±1.3	7.25±0.52	8.12±0.13	8.04±0.13	7.95±0.21
Vir A*	YY	8.39±0.69	6.4±1.3	6.74±0.72	6.110±0.076	6.196±0.077	6.29±0.10

Notes:
[1] – Observation from 2013-11-12 at azimuth 354.6°
[2] – Observation from 2013-09-26 at azimuth 5.5°
* – strong RFI peak around transit

Table 3: SEFDs derived from the beam-outrigger correlation. Errors are statistical only.

Target	Pol.	36	42	48	68	74	80
		MHz/kJy					
Cyg A	XX	2.07±0.29	1.32±0.13	1.60±0.11	2.10±0.57	1.392±0.089	2.08±0.46
Cyg A	YY	1.81±0.40	1.63±0.21	1.53±0.20	1.38±0.12	1.30±0.10	1.24±0.12
Cas A[1]	XX	3.78±0.41	4.23±0.39	2.40±0.24	1.60±0.17	1.70±0.12	2.21±0.12
Cas A[1]	YY	4.67±0.83	4.21±0.71	3.14±0.56	1.76±0.13	1.53±0.45	1.230±0.076
Cas A[2]	XX	1.60±0.17	1.47±0.14	1.92±0.17	1.57±0.16	3.94±0.87	2.20±0.67
Cas A[2]	YY	1.44±0.16	1.65±0.23	2.04±0.24	1.30±0.11	1.59±0.29	1.28±0.25
Tau A	XX	1.78±0.33	1.00±0.10	0.96±0.23	2.03±0.66	2.06±0.67	1.90±0.45
Tau A	YY	1.43±0.21	1.10±0.13	1.66±0.54	1.79±0.42	2.78±0.92	1.43±0.39
Vir A*	XX	1.1±2.0	0.64±1.80	0.63±0.90	0.94±0.18	4.5±3.5	1.58±0.46
Vir A*	YY	0.80±1.32	0.60±1.58	0.75±1.51	0.85±0.20	1.45±0.60	0.86±0.15

Notes:
[1] – Observation from 2013-11-12 at azimuth 354.6°
[2] – Observation from 2013-09-26 at azimuth 5.5°
* – strong RFI peak around transit and strong scintillation on outrigger baselines in the high tuning mainly at 74 MHz

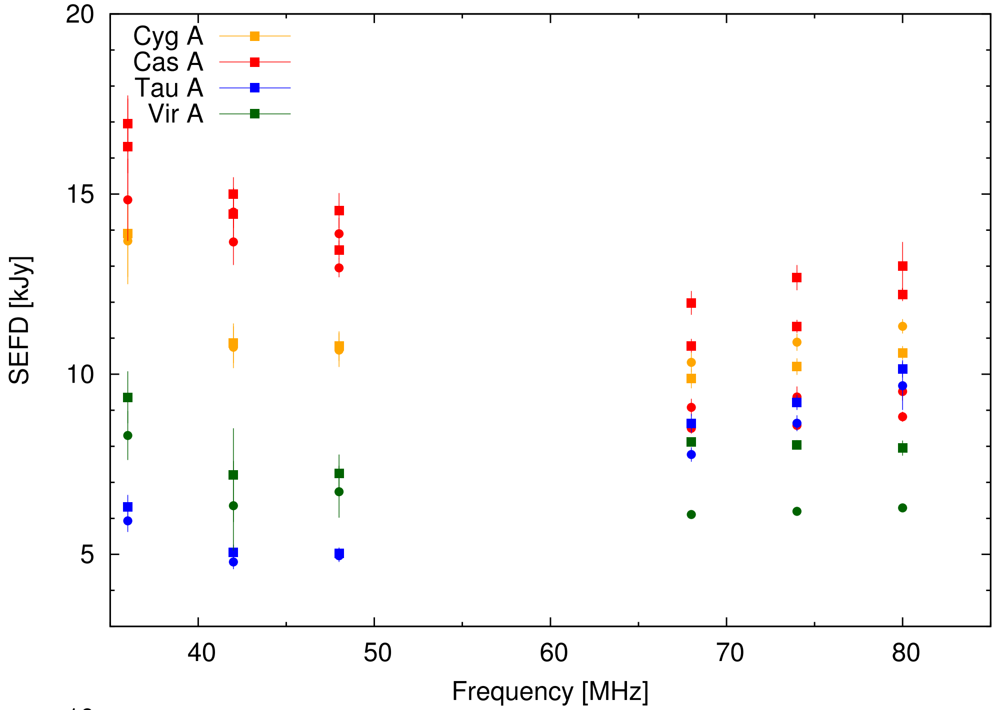

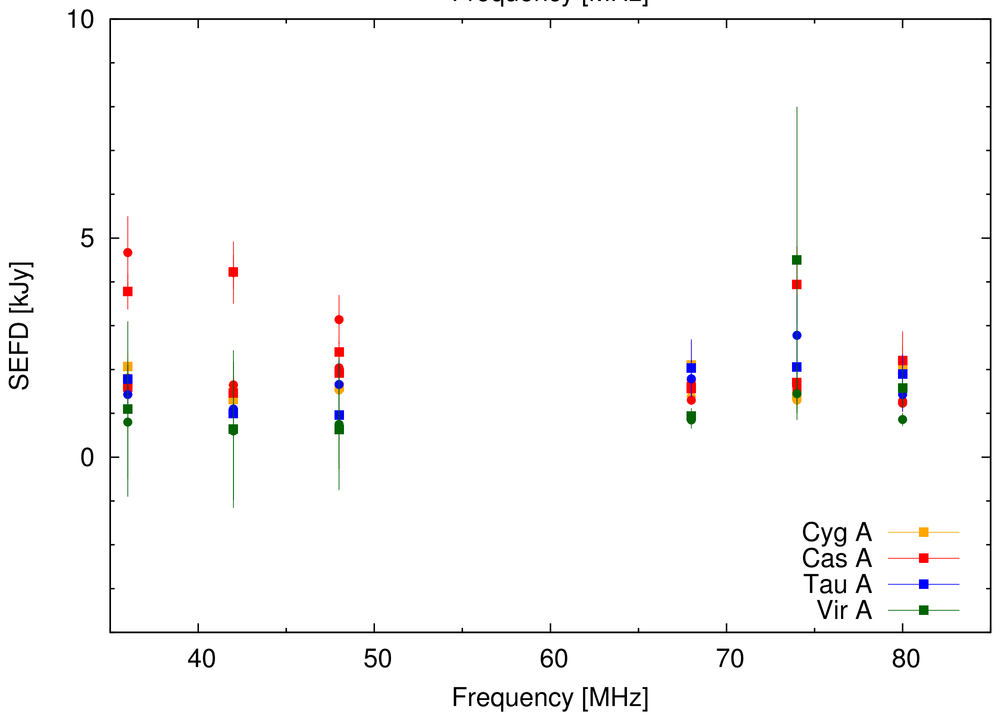

Figure 2: Top: Distribution of SEFD values for the beam-beam autocorrelation. Bottom: Distribution of SEFD values for the beam-outrigger correlation. The square symbols denote XX polarization, circles denote YY polarization.

beam-forming mode as well as with beam and outrigger correlations. An overview of the number of observations, the total observing time used and the fraction of compromised datasets are listed in Table 4. Datasets are marked as compromised if any of the following occurred: the drift scan did not fit properly, the recorded data were corrupted, strong RFI was present, or the ionosphere showed scintillations making the determination of power levels less reliable.

Table 4: Number of observations per elevation with custom beam-forming with the beam and the RTA outrigger (B+O) and regular beam-forming of the core station only (B only). The fraction of compromised observations due to RFI, ionosphere, or technical issues is given as well (*) and the total number of beam hours scheduled.

Cyg A	Elevation	25	30	35	40	45	50	55	60	65	70	75	80
	B+O	5	4	4	5	4	4	4	4	4	4	4	7
	(*) %	54	23	27	33	29	22	27	15	0	0	0	58
	B only	2	2	2	1	2	2	2	2	2	2	2	2
	(*) %	8.3	16.7	25	17	50.0	50	50	67	50	50	0	50
	hours	12	10	10	11	10	10	10	10	10	10	10	26
Cas A	Elevation	25	30	35	40	45	50	55	60	65			
	B+O	4	4	4	4	4	4	4	4	4			
	(*) %	29	15	2	10	14.5	0	6	0	3			
	B only	2	2	2	2	2	2	2	3	1			
	(*) %	0	0	0	0	0	0	0	0	83			
	hours	10	10	10	10	10	10	10	11	9			
Tau A	Elevation		30	35	40	45	50	55	60	65	70	75	
	B+O		2	1	2	2	3	2	1	2	2	4	
	(*) %		88	100	58	75	82	58	75	58	54	50	
	hours		4	2	4	4	6	4	2	4	4	8	
Vir A	Elevation	25	30	35	40	45	50	55	60	65			
	B+0	2	1	2	1	1	1	2	2	3			
	(*)	96	67	92	83	67	92	67	42	50			
	hours	4	2	4	2	2	2	4	4	6			

Notes:
(*) – fraction of compromised data

To evaluate and compare the change in power between different objects, the ratios between power levels determined from observations described in Section 2 (P_0) and those measured at different elevations (P_1) were used to scale the power changes relative to the reference elevations listed in Table 1. The relation between SEFD and noise power level can be expressed by the following equation:

$$P = g^2 \frac{\eta_a \cdot A}{2} SEFD\, \Delta\nu, \tag{2}$$

where g is the gain in voltage, η_a is the antenna efficiency[2], A is the antenna area, and $\Delta\nu$ is the observation bandwidth. The antenna pattern and thus its reflection on antenna efficiency was determined by Hartman (2009) using two-element interferometric experiments. It showed that the antenna gain drops by up to 6 dB between the zenith and 25° elevation.

The power measured from a source on the sky can be expressed in a similar way to that in Equation 2:

$$P_{\mathrm{sky}} = g^2 \frac{\eta_a \cdot A}{2} S\, \Delta\nu, \tag{3}$$

where all variables are the same as above and S corresponds to the total flux density of the observed sky. Since we are observing and comparing the same portion of the sky the value of S can be assumed to be source elevation independent. Between different observations the bandwidth, actual antenna area, A, as well as the system gain do not change. However, the value of η_a scales the same in both cases. The parameters are indicated by a subscript 0 for the reference elevation and at other elevations are indicated by a subscript 1. Thus we can calculate the noise power ratio of:

$$\frac{P_0}{P_1} = \frac{\eta_0}{\eta_1} \frac{SEFD_0}{SEFD_1}. \tag{4}$$

The SEFD at a different elevation than the reference elevation can then be obtained. The antenna power changes in a similar fashion, with which the ratio $\frac{\eta_0}{\eta_1}$ can be determined. This way we can use the power levels determined from observations of the same part of the sky to determine the SEFD at a different elevation than the reference elevation, for which we have obtained the SEFD (see Section 2), in the following way:

$$SEFD_1 = \frac{P_1}{P_0} \cdot \frac{\eta_0}{\eta_1} \cdot SEFD_0. \tag{5}$$

Under the assumption that the system noise power is approximately equivalent for both elevations ($P_1 \approx P_0$), we can use the measured sky power ratio together with the SEFD at the reference elevation, $SEFD_0$, to obtain an estimate for the SEFD value at the elevation we are interested in. Since $SEFD_0$ is merely a scaling factor and has a significant dependence on the part of the sky from which it was extracted (see Section 4) only the determined ratio η_0/η_1 is used for the following discussion of elevation dependence which, if necessary, can easily be scaled to any reference SEFD value.

Data were processed using custom scripts to extract the power levels from the drift scans and store resulting information, including metadata, into a relational database from which only data entries marked as uncompromised data were selected. Since multiple observations were taken per frequency and elevation the data was inspected before averaging[3] each

[2] The antenna efficiency is the ratio between directivity and gain of an antenna, which in the case of a beam-formed array is highly direction dependent.

[3] using a weighted average

elevation data point in order to ensure the integrity of the averaged data points. The spread of power levels observed were mostly found to be within statistical errorbars. After this the data used in the following discussion was compiled.

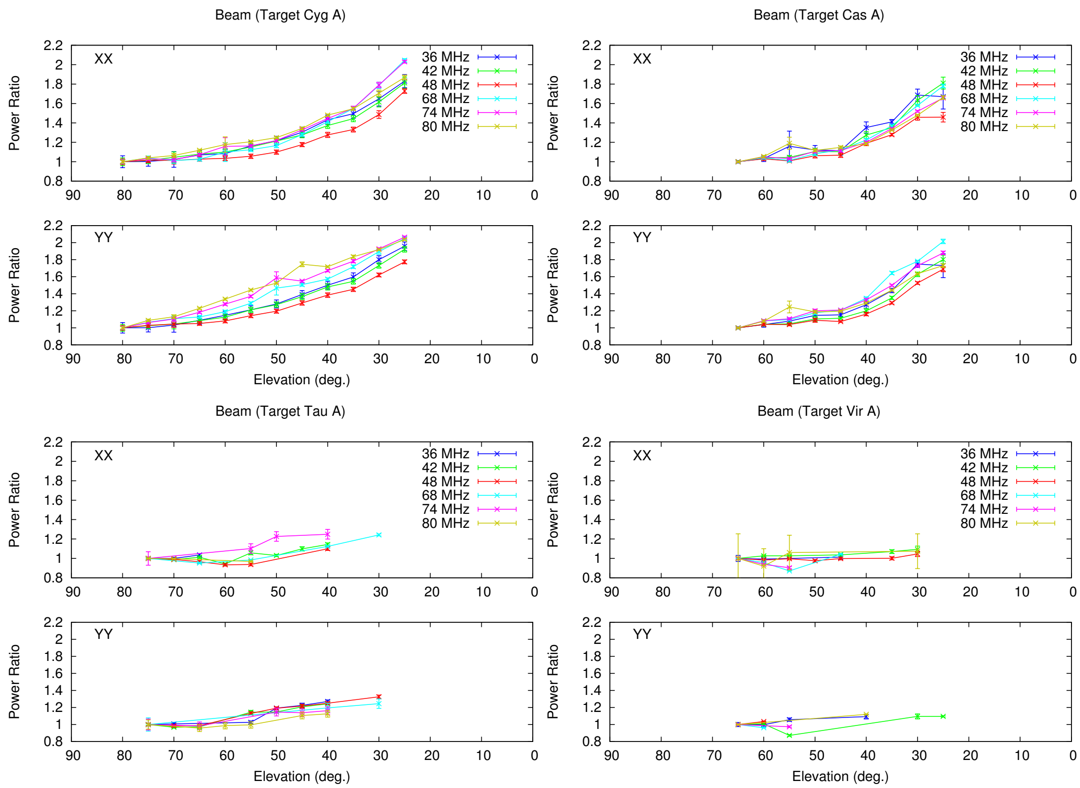

Figure 3: The elevation dependence of the power ratio for the beam observations is plotted for six select frequencies (36, 42, 48, 68, 74, and 80 MHz) for the observed objects, Cygnus A, Cassiopeia A, Taurus A, and Virgo A. Within each plot the top panel shows data for the XX polarization and the bottom panel shows the YY polarization.

Since this is a multi-dimensional dataset a first look was given to the frequency dependence of the change in signal power with elevation. For this the power for a given elevation is plotted against frequency. This is shown in Fig. 3 for the station beam and in Fig. 4 for the correlation between the station beam and the outrigger #4 dipole. From these plots it is evident that the power dependence with elevation follows mostly the same trend, within statistical errors, at all observed frequencies. However, in the case of the beam autocorrelations of Vir A and Tau A observations, this trend is not present, most likely due to a significant contribution of beam confusion. The change of sensitivity with elevation of both the beam and the beam-outrigger correlation is frequency independent. Moreover, the calculated power ratios are very similar between different frequencies, although some

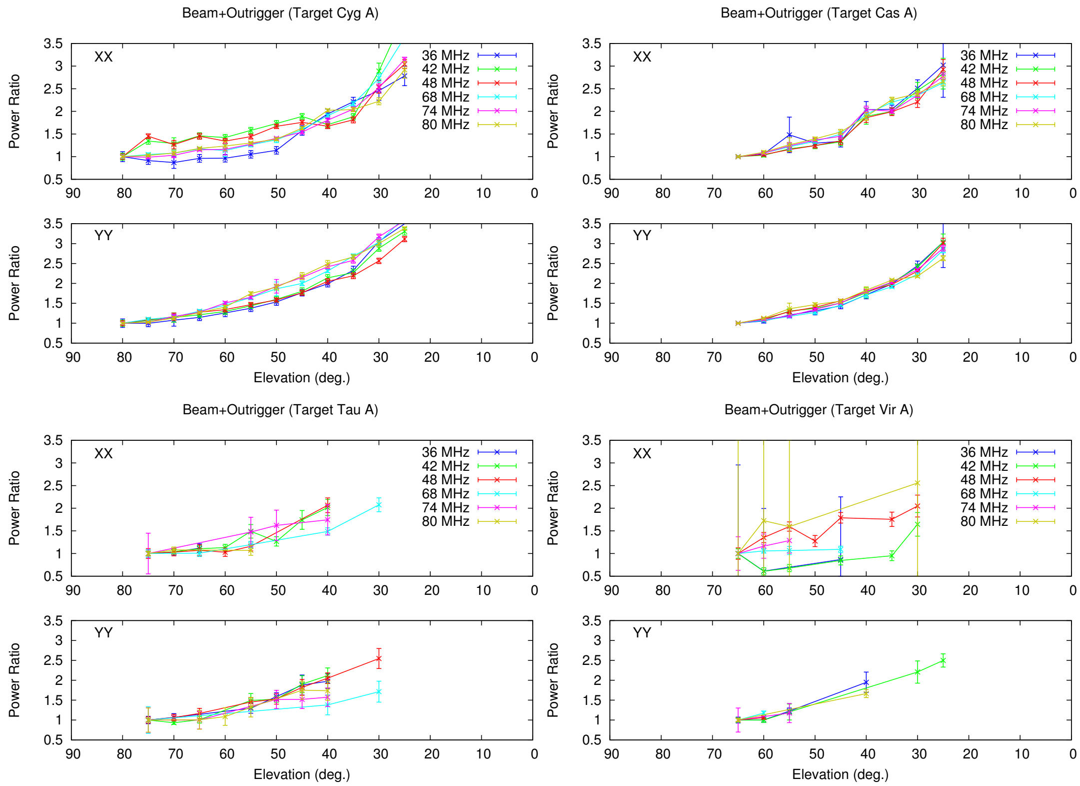

Figure 4: The elevation dependence of the power ratio for the beam-outrigger correlations is plotted for six select frequencies (36, 42, 48, 68, 74, and 80 MHz) for the observed objects, Cygnus A, Cassiopeia A, Taurus A, and Virgo A. Within each plot the top panel shows data for the XX polarization and the bottom panel shows the YY polarization.

spread can be seen in the case of the beam observations of Cygnus A. Nevertheless, for clarity of presentation, the weighted average across the power ratios determined at different frequencies is used to further characterize the elevation dependence of the sky power.

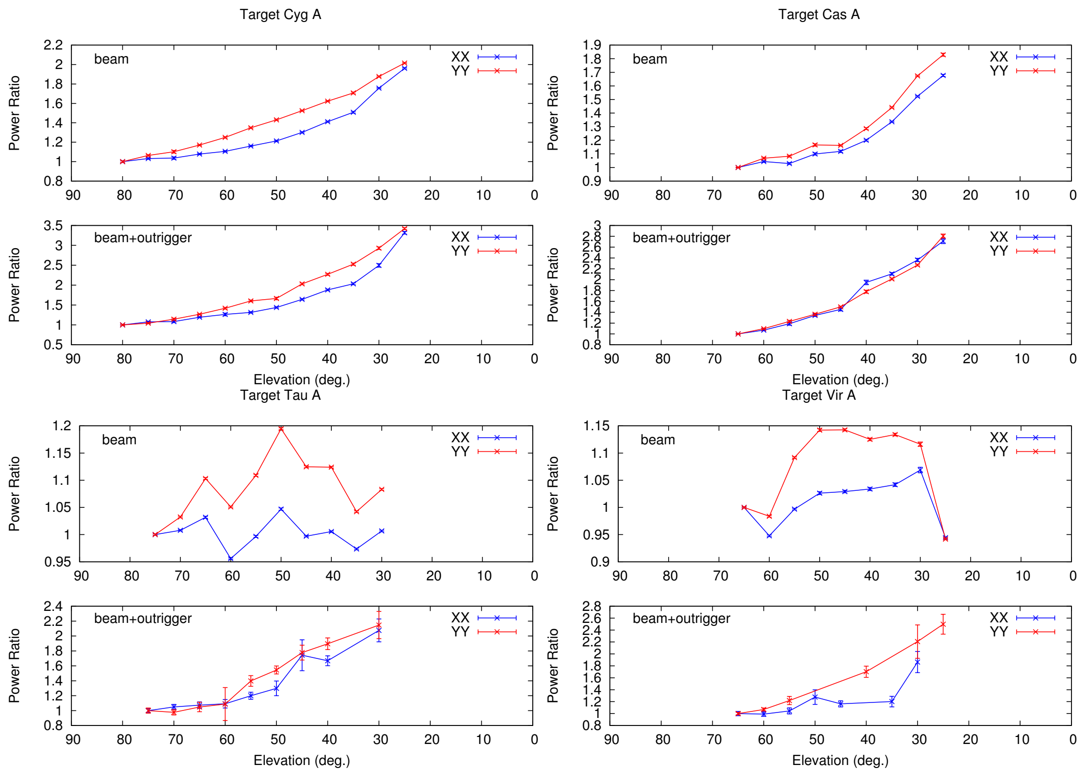

Figure 5: Frequency averaged elevation dependence of the power ratio for each of the four objects observed. The top panel in each plot shows the beam observation data, the bottom panel the beam-outrigger correlation.

In Fig. 5 the frequency averaged power ratios are plotted against source elevation. In all four sources the beam data shows a clear difference between the two polarization products, which is most likely source and LST dependent. In order to facilitate direct comparison of the power ratio elevation dependence between the observed objects, the curves from all four sources were scaled to that of the 65° elevation datapoint of Cygnus A. At elevations between 50 and 75 degrees the values of Cyg A and Tau A agree within less than 20%. However, at elevations less than 60° the power ratio values show significant differences from source to source. In the case of the beam-outrigger correlations the values obtained from different sources are mostly in good agreement.

For the beam autocorrelations of Cyg A and Cas A it was possible to fit a power-law dependence to both the XX and YY polarizations with the following parameters:

$$\eta(x) = a \cdot x^b + c, \tag{6}$$

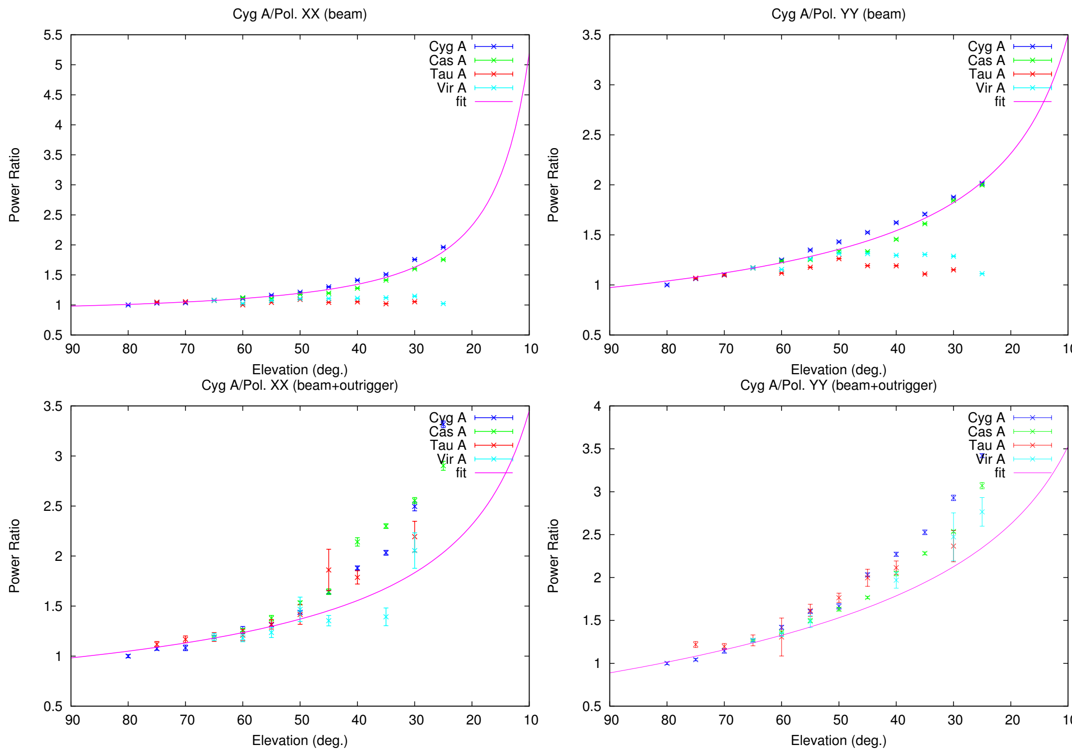

Figure 6: Frequency averaged elevation dependence of the power ratio plotted together for comparability. The different power ratios were scaled to that of Cygnus A at 65° elevation.

where x is the elevation angle in degrees, and the parameters a,b,c were determined to be $a = 155$, $b = -1.55$, $c = 0.84$ for XX polarization and $a = 14.1$, $b = -0.62$, $c = 0.10$ for YY polarization. The beam-outrigger power ratio clearly does not follow a power law dependence for elevations below 50°, the determined fit parameters were $a = 13.1$, $b = -0.58$, $c = 0.037$ for XX polarization and $a = 15.4$, $b = -0.115$, $c = -8.28$ for YY polarization. The curves were also fit using the following function from Ellingson (2011),

$$p(\theta) = \left[1 - \left(\frac{\theta}{\pi/2}\right)^{\alpha}\right] \cos^{\beta}\theta + \gamma \left(\frac{\theta}{\pi/2}\right) \cos^{\delta}\theta; 0 \leq \theta \leq \frac{\pi}{2}, \tag{7}$$

where θ is the zenith angle and $\alpha, \beta, \gamma, \delta$ are fit parameters. The resulting fits were equal to those of the power-law fit function with only three free parameters.

4 Sky Power Changes with LST

This section addresses the change in beam sensitivity due to the interplay of sky noise correlation with diffuse sky emission. In Section 2 it was shown that the SEFD values determined for the beam are at least a factor of 2 worse than what was found for the beam-outrigger baseline demonstrating the significance of this effect. For this a number of 24 hour observations were conducted to observe the change in beam power over the entire LST range. Unfortunately, some of these observations were impacted by strong solar activity and interruptions by regular science observations. The best continuous dataset was captured on December 25, 2013 using a reduced sampling rate (DP filter code 3) providing a maximum bandwidth of 1 MHz per tuning. The tunings were centered at 42.0 and 74.0 MHz. Two beams were recorded simultaneously with one fixed at zenith (90° elevation) and the second fixed at the Northern celestial pole (34° elevation) allowing the sky to drift by over the 24 hour period.

Without the additional information of absolute flux density of the station beam it is impossible to transfer either flux density or determine the time variability of the station sensitivity accurately. However, if we make the assumption that the off-beam is the same for both the calibrator source and the part of the sky we want to bootstrap the flux density for and the SEFD is known for the two parts of the sky, then it is possible to calculate:

$$S_{\text{target}} = S_{\text{ref}} \frac{P_{\text{target}}}{P_{\text{ref}}} \cdot \eta, \tag{8}$$

where S_{ref} is the flux density of the calibrator, P_{ref} is the measured beam power of the calibrator, P_{target} is the observed beam power for the patch of the sky for which the flux density is to be determined, and η is the ratio (η_0/η_1) determined in Section 3 that adjusts the difference in SEFD for different elevations. This crude method is more accurate the closer the target field is to the calibrator. Since the 24 hour observation was recorded with different observing parameters than for the drift scan observations, a separate drift scan on Cygnus A at 80° elevation (LST 20:37) was recorded on January 01, 2014 to provide

Table 5: Values used for calibrating the 24 hour pointings on zenith and the Northern celestial pole at LST 20:37.

Target	Pol.	42 MHz			74 MHz		
		S (kJy)	P_{on}	η	S (kJy)	P_{on}	η
Cyg A	XX	24.046	32.82	-	17.250	11.44	-
	YY	24.046	33.53	-	17.250	12.62	-
Zenith	XX	**11.9**	16.06	1.01	**7.9**	5.17	1.01
	YY	**11.3**	15.42	1.02	**7.5**	5.36	1.02
NCP	XX	**18.0**	16.25	1.51	**12.0**	5.26	1.51
	YY	**19.0**	15.65	1.69	**13.2**	5.73	1.69

values for P_{ref}. The values used for calibration of flux densities are listed in Table 5. The limiting factor for this method is that the value at S_{ref} needs to be known. Here we made the assumption that we can measure the sky power when the emission of Cygnus A dominates. However, due to the large diameter of the beam on the sky a significant fraction of additional sky brightness contributes to the power so that the assumption that $S_{\mathrm{ref}} = S_{\mathrm{CygA}}$ provides only an upper limit for the true flux density. If 50% of the beam power were contributed from sidelobes, then the flux density values determined for zenith and NCP would be a factor of 2 smaller. With this note of caution on the interpretation of the bootstrapped flux density values, the observed sky power is plotted against LST for 42 and 74 MHz in Fig. 7 using the scaling parameters from Table 5. Small scale ripples that were introduced from variations in the shelter electronics temperature caused by the air conditioning units cycling were removed, for more information see Schinzel (2013).

A few observations can be made from these plots. The observed power levels, especially at 74 MHz, are similar no matter whether pointing at the zenith or NCP. The bootstrapped flux density levels suggest that the total power observed at lower elevations is greater compared to zenith observations, which is due to the measured drop in sensitivity toward lower elevations. This suggests a significant sidelobe contribution at lower elevations.

5 Summary & Conclusions

In this memo observations were discussed that were conducted with the aim to obtain a better understanding of the station sensitivity with the goal to provide some guidelines for the absolute flux calibration of astronomical observations conducted with LWA1 including possible caveats. At this point accurate absolute flux calibration is not possible without the additional knowledge of the sky, sidelobes and other instrumental effects that contribute to the measured power. Future work will address this by providing simulations using existing sky models providing anchor points to the observed flux density of the sky.

In summary the following conclusions were drawn from the analysis of the observations presented here:

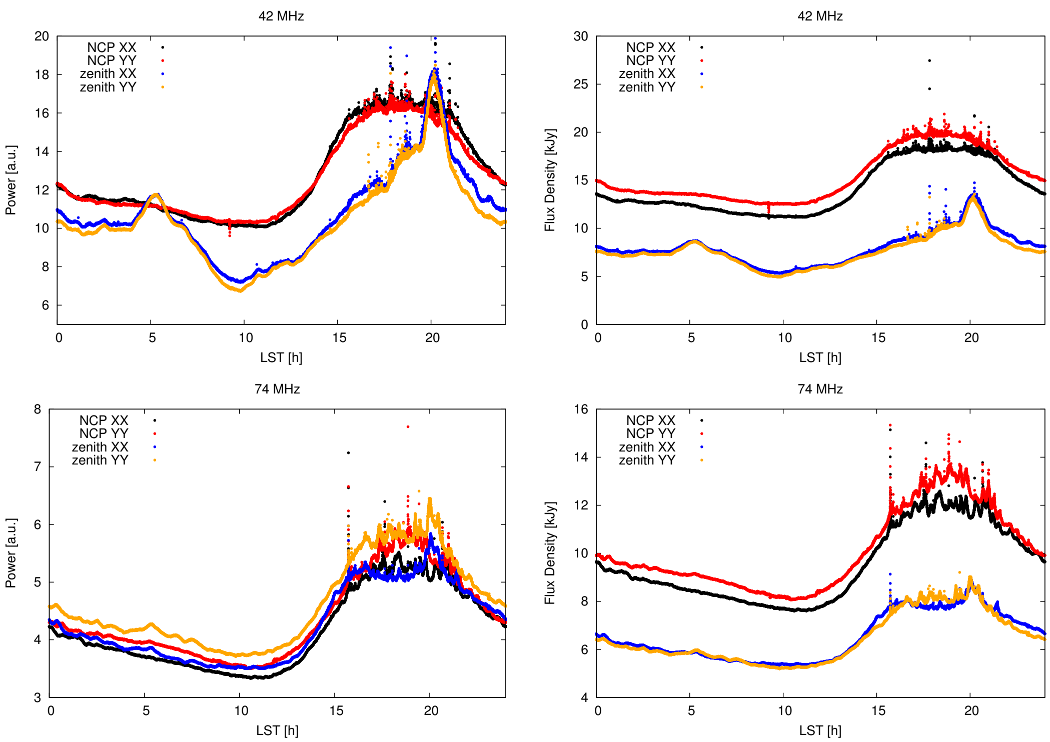

Figure 7: LST dependence of the observed sky power for pointing the beam at zenith and at NCP. The plots on the top show the LST dependence for 42 MHz and the plots for 74 MHz are shown on the bottom. Plots on the left show the uncalibrated observed power, plots on the right are scaled to the bootstrapped flux density levels.

- The SEFD change across frequency is negligible within the probed frequency range of 36 - 80 MHz, although a drop toward the band edges at 36 and 80 MHz is noticeable in some cases since the ASP split bandwidth filter was used for all observations.
- Beam-outrigger correlation reduces the SEFD by about a factor of 7, reducing the influence of diffuse sky emission.
- The change in sensitivity of the beam with elevation across frequency is negligible as expected when there is no frequency dependence of the SEFD.
- The observed elevation dependences do not allow generalization across sources or polarizations however it was found that for the beam the observed elevation dependence is similar for all sources above 60 degrees elevation, whereas for the beam+outrigger correlation a similar dependence was found for all probed sources and elevation ranges.
- The power-elevation dependence of Cyg A and Cas A is well described by a powerlaw between 25 and 80° for the beam auto-correlation. However, for the beam-outrigger baselines the power ratio does not follow a powerlaw below 60° elevation.
- A 24 hour observation pointing the station beam at zenith and NCP shows a significantly different power between LST 12 and LST 19 when the Galactic plane is up. An attempt was made to bootstrap flux density values for this observation providing upper limits for the observed flux density.

References

Ellingson, S. 2011, Antennas and Propagation, IEEE Transactions on, 59, 1855

Ellingson, S., Taylor, G., Craig, J., et al. 2013, Antennas and Propagation, IEEE Transactions on, 61, 2540

Hartman, J. 2009, Antenna pattern measurements from the two-element interferometer, LWA Memo 155

Helmboldt, J. F. & Kassim, N. E. 2009, The Astronomical Journal, 138, 838

Schinzel, F. 2013, The Influence of Shelter Temperature on Gain Stability of LWA1, LWA Memo 198

Acknowledgement

We thank Sean Cutchin for the discussions and support surrounding the SEFD work and related observations in custom beamforming mode.